

Imaging the energy gap modulations of the cuprate pair-density-wave state

<https://doi.org/10.1038/s41586-020-2143-x>

Received: 15 August 2019

Accepted: 20 January 2020

Published online: 1 April 2020

 Check for updates

Zengyi Du^{1,7}, Hui Li^{1,2,7}, Sang Hyun Joo³, Elizabeth P. Donoway^{1,4}, Jinho Lee³, J. C. Séamus Davis^{5,6}, Genda Gu¹, Peter D. Johnson¹ & Kazuhiro Fujita^{1,3,8}

The defining characteristic^{1,2} of Cooper pairs with finite centre-of-mass momentum is a spatially modulating superconducting energy gap $\Delta(\mathbf{r})$, where \mathbf{r} is a position. Recently, this concept has been generalized to the pair-density-wave (PDW) state predicted to exist in copper oxides (cuprates)^{3,4}. Although the signature of a cuprate PDW has been detected in Cooper-pair tunnelling⁵, the distinctive signature in single-electron tunnelling of a periodic $\Delta(\mathbf{r})$ modulation has not been observed. Here, using a spectroscopic technique based on scanning tunnelling microscopy, we find strong $\Delta(\mathbf{r})$ modulations in the canonical cuprate $\text{Bi}_2\text{Sr}_2\text{CaCu}_2\text{O}_{8+\delta}$ that have eight-unit-cell periodicity or wavevectors $\mathbf{Q} \approx (2\pi/a_0)(1/8, 0)$ and $\mathbf{Q} \approx (2\pi/a_0)(0, 1/8)$ (where a_0 is the distance between neighbouring Cu atoms). Simultaneous imaging of the local density of states $N(\mathbf{r}, E)$ (where E is the energy) reveals electronic modulations with wavevectors \mathbf{Q} and $2\mathbf{Q}$, as anticipated when the PDW coexists with superconductivity. Finally, by visualizing the topological defects in these $N(\mathbf{r}, E)$ density waves at $2\mathbf{Q}$, we find them to be concentrated in areas where the PDW spatial phase changes by π , as predicted by the theory of half-vortices in a PDW state^{6,7}. Overall, this is a compelling demonstration, from multiple single-electron signatures, of a PDW state coexisting with superconductivity in $\text{Bi}_2\text{Sr}_2\text{CaCu}_2\text{O}_{8+\delta}$.

The exact nature of the cuprate pseudogap state⁸ has been the focus of extensive research as a route to understanding high-temperature superconductivity. Attention has recently focused on a pair-density-wave (PDW) state^{3,4} as a leading candidate to be the fundamental order parameter that characterizes the pseudogap. This was originally motivated by transport studies⁹, which led to the hypothesis of ‘stripe superconductivity’, in which the superconducting order parameter is spatially modulated and thus a PDW^{10,11}. Equally, the highly unusual band structure reconstruction near the pseudogap opening temperature T^* as observed by angle-resolved photoemission spectroscopy¹² can be explained relatively simply by the formation of a PDW state^{13,14}. Indeed, a wide variety of microscopic theories based on strong, local electron–electron interactions now envisage a copper oxide (cuprate) PDW state^{15–22}, while experimental evidence for its existence is rapidly emerging from multiple techniques^{4,5,23,24}.

Characteristic signatures in single-electron tunnelling of the PDW state

Here we focus on the challenge of detecting the cuprate PDW state using single-electron tunnelling. First, we consider a PDW, whose spatially dependent energy gap is $\Delta(\mathbf{r}) = F_p \Delta_Q^p [e^{i\mathbf{Q}\cdot\mathbf{r}} + e^{-i\mathbf{Q}\cdot\mathbf{r}}]$, where Δ_Q^p is the amplitude of gap modulations at wavevector \mathbf{Q} , \mathbf{r} is a position and F_p is the form factor with either s - or d -symmetry. The most obvious and immediate prediction is that the single-electron tunnelling should

detect a gap in the density-of-states spectrum $N(E)$ (where E is energy), which modulates at \mathbf{Q} . It is striking, therefore, that no such modulating $\Delta(\mathbf{r})$ has ever been observed in the cuprates. Second, if such a PDW coexists with d -wave superconductivity (SC), whose homogeneous gap is $\Delta^s(\mathbf{r}) = F_{SC} \Delta^s$, where F_{SC} exhibits d -symmetry, then Ginzburg–Landau theory predicts the form of $N(\mathbf{r}, E)$ modulations generated by the interactions between the PDW $\Delta(\mathbf{r})$ and the superconducting $\Delta^s(\mathbf{r})$. These modulations are identifiable from products of these two order parameters that transform as density-like quantities. Thus, considering the product of the PDW and SC order parameters, $\Delta_Q^p \Delta^s$ predicts $N(\mathbf{r}) \propto \cos(\mathbf{Q}\cdot\mathbf{r})$ modulations at the PDW wavevector \mathbf{Q} , while the product of a PDW with itself $\Delta_Q^p \Delta_Q^p$ predicts $N(\mathbf{r}) \propto \cos(2\mathbf{Q}\cdot\mathbf{r})$ at twice the PDW wavevector. Therefore, a second unique signature of a PDW with wavevector \mathbf{Q} in the superconducting cuprates would be the coexistence of two sets of $N(\mathbf{r}, E)$ modulations at \mathbf{Q} and $2\mathbf{Q}$. Finally, a topological defect with 2π phase winding²⁵ in the induced density wave $N(\mathbf{r}) \propto \cos(2\mathbf{Q}\cdot\mathbf{r})$ is predicted to generate a local phase winding of π in the PDW order, at a half-vortex⁶ (Fig. 1a). This is the topological signature of a PDW coexisting with homogeneous SC. Experimental detection of these phenomena in single-electron tunnelling would constitute compelling evidence for the PDW state.

To explore these predictions, we use spectroscopic imaging scanning tunnelling microscopy²⁶ (SI-STM) with a $\text{Bi}_2\text{Sr}_2\text{CaCu}_2\text{O}_{8+\delta}$ nano-flake tip⁵ to visualize the single-electron tunnelling. Utilization of the superconducting tip enhances the energy resolution due to the

¹CMPMS Department, Brookhaven National Laboratory, Upton, NY, USA. ²Department of Physics and Astronomy, Stony Brook University, Stony Brook, NY, USA. ³Department of Physics and Astronomy, Seoul National University, Seoul, Republic of Korea. ⁴Department of Physics, University of California, Berkeley, Berkeley, CA, USA. ⁵Department of Physics, University College Cork, Cork, Ireland. ⁶Clarendon Laboratory, University of Oxford, Oxford, UK. ⁷These authors contributed equally: Zengyi Du, Hui Li. ⁸e-mail: kfujita@bnl.gov

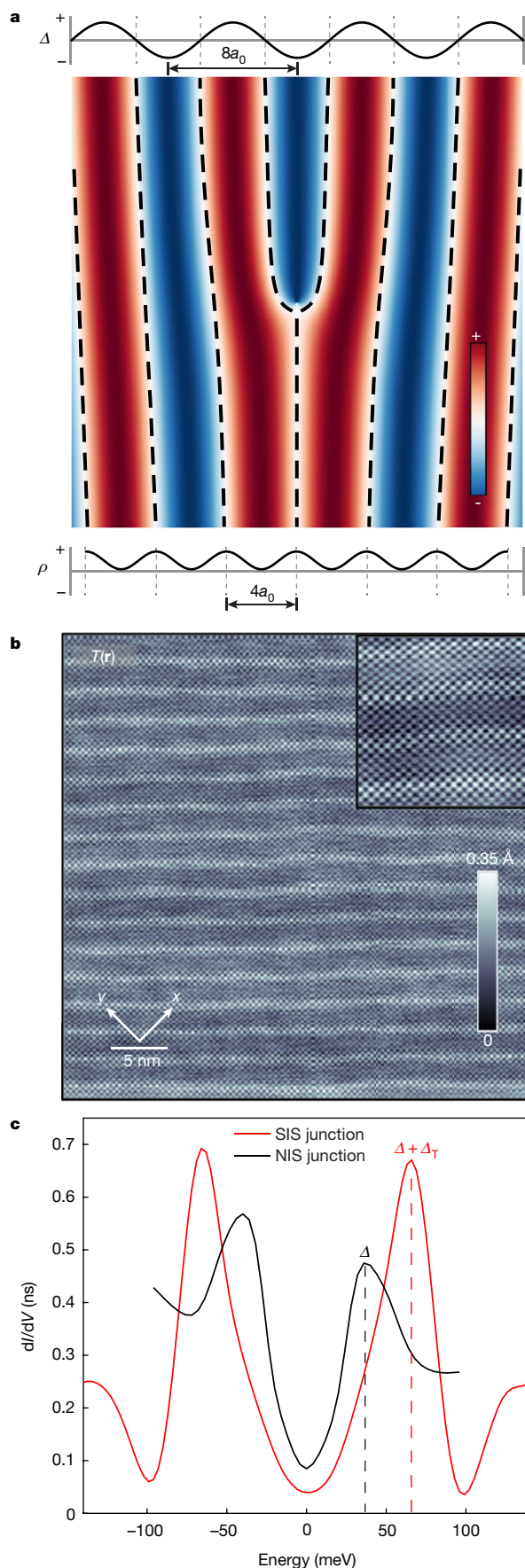


Fig. 1 | Schematic of unidirectional $8a_0$ PDW order intertwined with a density wave. **a**, Unidirectional PDW order parameter is modulated along the horizontal axis at eight-unit-cell periodicity. The sign of $\Delta(\mathbf{r})$ is coloured in red for positive and in blue for negative. The periodicity in the unidirectional density-of-electronic-states $N(\mathbf{r})$ detectable by NIS tunnelling, which is intertwined with unidirectional PDW, is depicted by a black broken line. The $N(\mathbf{r})$ wavelength is half that of the unidirectional PDW. When a dislocation occurs in unidirectional $N(\mathbf{r})$, where the 2π phase winding is realized in its phase, a possible fluctuation in unidirectional PDW order amplitude and/or half-vortices is predicted. The relative phase of the spatial variations in the PDW order and the induced density-wave modulations in $N(\mathbf{r})$ are also plotted at the top and bottom, respectively. **b**, Typical SIS topography of $\text{Bi}_2\text{Sr}_2\text{CaCu}_2\text{O}_{8+\delta}$ within $40\text{ nm} \times 40\text{ nm}$ FOV at $5\text{ G}\Omega$ junction resistance ($I = 30\text{ pA}$ at $V_{\text{bias}} = 150\text{ meV}$). Cu–O–Cu bond directions are parallel to the x and y axes. Individual Bi atoms are clearly observed as shown in the inset with intra-unit-cell resolution. **c**, Spatially averaged SIS $g(\mathbf{r}, E)$ spectrum (red) together with that taken with NIS junction (black). The spatially averaged SIS $g(\mathbf{r}, E)$ spectrum shows particle–hole symmetric peaks with energies at $E = \pm 66\text{ meV}$. As the spatially averaged NIS $g(\mathbf{r}, E)$ peaks at $\pm 37\text{ meV}$, we estimate the average gap value on the $\text{Bi}_2\text{Sr}_2\text{CaCu}_2\text{O}_{8+\delta}$ nanoflake tip, Δ_T , to be about 29 meV .

convolution of spectra that sharply peak at the superconducting gap edge, in the density of states $N_T(E)$ of the tip and $N(\mathbf{r}, E)$ of the sample. Thus, energy sensitivity to modulations in $\Delta(\mathbf{r})$ should be enhanced with this superconductor–insulator–superconductor (SIS) tunnelling technique. To enable detection of the gap modulation, a bulk single-crystal sample of $\text{Bi}_2\text{Sr}_2\text{CaCu}_2\text{O}_{8+\delta}$ at the hole density $p \approx 0.17 \pm 0.01$ (the error approximately corresponds to a transition width) and superconducting transition temperature $T_c = 91\text{ K}$ is cleaved at room temperature under ultrahigh vacuum conditions (3×10^{-10} torr) and then inserted into the cryogenic STM head. The superconducting tip is created by picking up a nanometre-scale $\text{Bi}_2\text{Sr}_2\text{CaCu}_2\text{O}_{8+\delta}$ flake from the sample⁵ to form the SIS junction. The SI-STM measurements throughout this study are then all performed using such SIS junctions at $T = 9\text{ K}$. A typical SIS topography is shown in Fig. 1b for a $40\text{ nm} \times 40\text{ nm}$ field of view (FOV). The individual Bi atoms in the BiO plane with subatomic resolution are resolved as shown in the inset. The CuO_2 plane exists about 6 \AA below the BiO plane.

Direct visualization of the periodic energy gap modulations

Differential SIS conductance spectra $g(\mathbf{r}, E) \equiv dI/dV(\mathbf{r}, E = eV)$, where I is the tunnelling current, V is the bias voltage and e is the elementary charge are then measured as a function of position in this FOV for the energy range from -150 meV to $+150\text{ meV}$. A typical such spatially averaged $g(\mathbf{r}, E)$ spectrum is shown in red in Fig. 1c, together with a normal-insulator–superconductor metal (NIS) spectrum performed earlier on the same sample but in a different FOV. The SIS $g(\mathbf{r}, E)$ spectrum, being a convolution of the tip $N_T(E)$ and sample $N(E)$ demonstrates enhanced energy resolution as expected (red in Fig. 1c). Here, as the spatially averaged NIS $g(\mathbf{r}, E)$ spectrum peaks at $\pm 37\text{ meV}$, while the equivalent SIS spectrum peaks at $\pm 66\text{ meV}$, we estimate the average energy gap of the tip Δ_T to be 29 meV .

Next, by measuring half the magnitude of the energy that separates the SIS spectrum peaks at every location, and then subtracting Δ_T , we determine the local gap energy map $\Delta(\mathbf{r})$ in the sample. A typical example is shown in Fig. 2a. Figure 2b shows the magnitude of the power-spectral-density Fourier transform $\Delta(\mathbf{q})$ of $\Delta(\mathbf{r})$ from Fig. 2a, where \mathbf{q} is a wavevector. Equivalent results have been achieved using SIS tunnelling with three different $\text{Bi}_2\text{Sr}_2\text{CaCu}_2\text{O}_{8+\delta}$ nanoflake tips, on three different samples and with two different STMs (Methods section ‘Motivation of searches for a PDW signature in $\Delta(\mathbf{r})$ ’). In Fig. 2b, \mathbf{q}_{SM} corresponds to a wavevector of the crystal-structure supermodulation. This supermodulation does indeed produce a type of PDW detectable

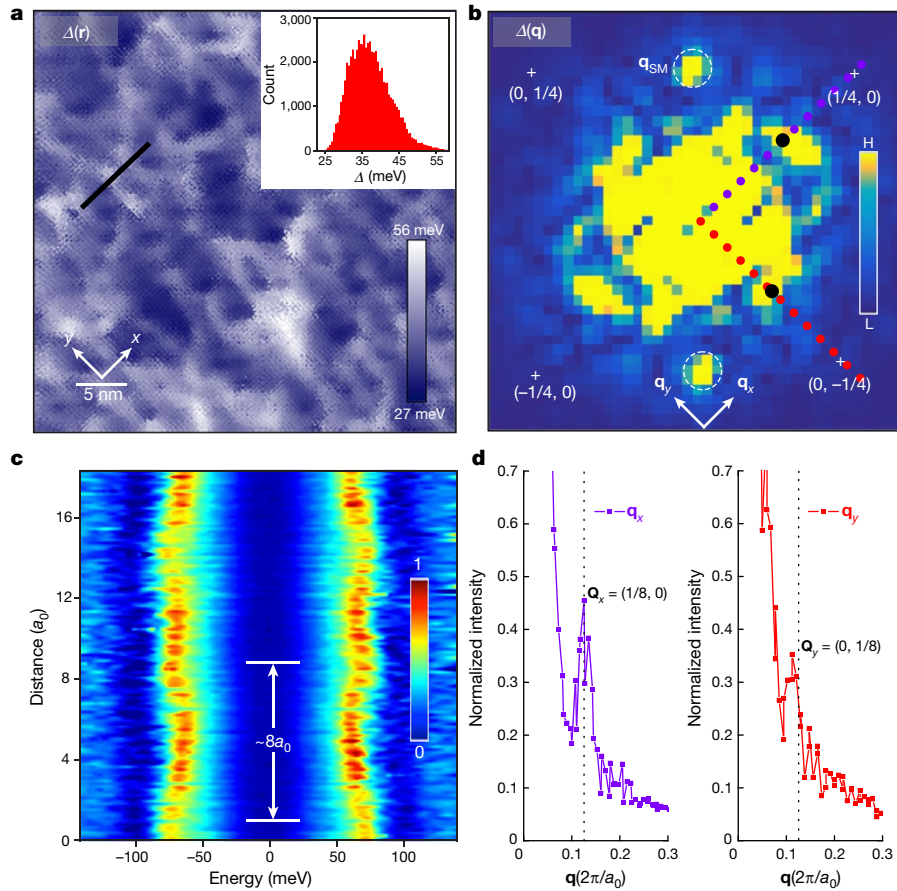


Fig. 2 | Superconducting gap energy modulations. **a**, Measured $\Delta(\mathbf{r})$ within $40 \text{ nm} \times 40 \text{ nm}$ FOV. The energy-gap data presented here and throughout the manuscript are all the measured values of the magnitude of $\Delta(\mathbf{r})$, which is half the energy separation between the coherence peaks minus the gap value of the $\text{Bi}_2\text{Sr}_2\text{CaCu}_2\text{O}_{8+\delta}$ nanoflake tip. The inset shows a distribution of measured $\Delta(\mathbf{r})$ in the same FOV, ranging from 27 to 56 meV. The eight-unit-cell modulation is clearly resolved in $\Delta(\mathbf{r})$, primarily running along the x direction of Cu–O–Cu bond exhibiting the unidirectional signature of the PDW. **b**, The magnitude Fourier transform of **a**. Well defined Fourier peaks at $\mathbf{Q} \approx (2\pi/a_0)(\pm 1/8, 0)$ and

$\mathbf{Q} \approx (2\pi/a_0)(0, \pm 1/8)$, corresponding to the eight-unit-cell modulations for both the x and y directions, are observed. H and L denote high and low, respectively. **c**, The series of SIS $g(\mathbf{r}, E)$ spectra intensity along the line in **a**. The eight unit-cell modulation of the energies of the coherence peaks is clearly resolved. The modulation amplitude is about 6 meV. **d**, The line cut of $|\Delta(\mathbf{q})|$ along both x and y directions from **b**. As seen in **b**, $\mathbf{Q}_x \approx (2\pi/a_0)(\pm 1/8, 0)$ and $\mathbf{Q}_y \approx (2\pi/a_0)(0, \pm 1/8)$ peaks are present for both directions, but a peak height is about twice larger for x than that for y direction indicating that the PDW is rather unidirectional.

by its energy gap modulations; but this PDW is trivial, occurring due to modulation of the crystal unit-cell dimensions (Methods section ‘Effect of structural supermodulation on measured $\Delta(\mathbf{r})$ ’). Second, there is a very broad peak in $\Delta(\mathbf{q})$ surrounding $\mathbf{q} = 0$ due to the well known random energy-gap disorder of $\text{Bi}_2\text{Sr}_2\text{CaCu}_2\text{O}_{8+\delta}$, and this is equivalent to the broad range of gap values in the histogram inset to Fig. 2a. Finally, there are four distinct local maxima in $\Delta(\mathbf{q})$ at the points indicated by black solid dots surrounding $\mathbf{q} \approx (0, \pm 0.125)$ and $\mathbf{q} \approx (\pm 0.125, 0)(2\pi/a_0)$, where a_0 is the periodicity.

These features indicate that there is a strong, if disordered, modulation in $\Delta(\mathbf{r})$, running parallel to the Cu–O–Cu bonds of the CuO_2 plane. This modulation exists on top of a non-periodic energy gap of about 37 meV. It exhibits well defined peaks at $\mathbf{Q}_x \approx (2\pi/a_0)(1/8, 0)$ and $\mathbf{Q}_y \approx (2\pi/a_0)(0, 1/8)$ meaning that $\Delta(\mathbf{r})$ is modulating with about $8a_0$ periodicity along both axes. Such a variation in $\Delta(\mathbf{r})$ can be seen directly in a series of SIS $g(\mathbf{r}, E)$ spectra, extracted along the line in Fig. 2a and shown in Fig. 2c. Here we see a local demonstration of the energy of maximum $N(\mathbf{r})$ (that is, of the coherence peak) modulating at about $8a_0$ periodicity in a particle–hole symmetric fashion with an amplitude of approximately 6 meV. More fundamentally, line profiles from $\Delta(\mathbf{q})$ in Fig. 2b are plotted in Fig. 2d for both directions. The two well defined peaks in Fig. 2d characterize a PDW with wavevectors $\mathbf{Q}_x \approx (0.129 \pm 0.003, 0)$ and $\mathbf{Q}_y \approx (2\pi/a_0)(0, 0.118 \pm 0.003)$. This is an

observation of coherent modulation in the superconducting energy gap $\Delta(\mathbf{r})$, and is precisely what is expected for a PDW state. Moreover, it reveals directly that the cuprate PDW occurs at wavevectors $\mathbf{Q} \approx (2\pi/a_0)(1/8, 0)$ and $\mathbf{Q} \approx (2\pi/a_0)(0, 1/8)$.

Relationship to PDW visualization using scanned Josephson tunnelling microscopy

Using the same $\text{Bi}_2\text{Sr}_2\text{CaCu}_2\text{O}_{8+\delta}$ nanoflake tip technology, on samples at the same doping as herein but operating at millikelvin temperatures, the magnitude of the Josephson current $|J_J(\mathbf{r})|$ is found to modulate with a wavelength of about $4a_0$. Thus, modulations of $|J_J(\mathbf{r})|$ and of $\Delta(\mathbf{r})$ are both detectable when using nanoflake tips that are extracted from the same crystal that is being studied, and are likely in the same coexisting SC and PDW state. Because the nanoflake tip is extended, an approximation to planar tunnelling must be considered. Here I_J from an extended tip to the crystal is composed of two contributions: I_J^S due to pair tunnelling from $c_k^\dagger c_{-k}^\dagger$ to $c_k^\dagger c_{-k}^\dagger$ states, and I_J^P due to pair tunnelling from $c_k^\dagger c_{k+Q}^\dagger$ to $c_k^\dagger c_{k+Q}^\dagger$ states, where c_k^\dagger is an electron creation operator at a momentum k , which are independent of each other when pair momentum is conserved (Methods section ‘Independent pair tunnelling process’). In scanned Josephson tunnelling microscopy, the circuitry measures the magnitude of Josephson critical current

Article

magnitude: $|J| = |J^S| + |J^P|$, for which $|J^S|$ is a roughly constant spatially but $|J^P| \propto |\sin(Q_p \delta)|$ where δ is the spatial displacement between the PDW in the extended tip and the PDW in the sample (Methods section ‘Independent pair tunnelling process’). Under these circumstances, if the PDW has periodicity $8a_0$, its gap modulates with periodicity $8a_0$, but the magnitude of the total Josephson current $|J|$ will have periodicity $4a_0$. This is the specific phenomenology detectable using the $\text{Bi}_2\text{Sr}_2\text{CaC}_2\text{O}_{8+\delta}$ nanoflake tips for SIS spectroscopy and to measure the magnitude of Josephson critical currents⁵, respectively. Furthermore, enhanced sensitivity to the basic energy modulations when using SIS spectroscopy is consistent with a ‘lock-in’ effect from a PDW state in the nanoflake tip (Methods section ‘Effect of $\Delta(\mathbf{r})$ on nanoflake’).

Detection of two unidirectional PDWs within distinct nanoscale domains

Next, to explore the unidirectionality of $\Delta(\mathbf{r})$, we employ a two-dimensional lock-in technique to determine the amplitude and phase of the modulations²⁷. Thus

$$A_{\mathbf{Q}}(\mathbf{r}) = \int d\mathbf{R} A(\mathbf{R}) e^{i\mathbf{Q}\cdot\mathbf{R}} e^{-\frac{(\mathbf{r}-\mathbf{R})^2}{2\sigma^2}} \quad (1)$$

$$|A_{\mathbf{Q}}(\mathbf{r})| = \sqrt{\text{Re}A_{\mathbf{Q}}(\mathbf{r})^2 + \text{Im}A_{\mathbf{Q}}(\mathbf{r})^2} \quad (2)$$

$$\Phi_{\mathbf{Q}}^A(\mathbf{r}) = \tan^{-1} \frac{\text{Im}A_{\mathbf{Q}}(\mathbf{r})}{\text{Re}A_{\mathbf{Q}}(\mathbf{r})} \quad (3)$$

where $A(\mathbf{r})$ represents any arbitrary real space image, \mathbf{Q} the wavevector of interest and σ the averaging length-scale in r -space (or equivalently the cut-off length in q -space). The key ingredients of such an analysis are the amplitude $|A_{\mathbf{Q}}(\mathbf{r})|$ and the spatial phase $\Phi_{\mathbf{Q}}^A(\mathbf{r})$ of modulations at \mathbf{Q} . Using this technique on our $\Delta(\mathbf{r})$ data, Fig. 3a, b shows the amplitudes of the PDW for the x and y directions, $|\Delta_{\mathbf{Q}_x}(\mathbf{r})|$, $|\Delta_{\mathbf{Q}_y}(\mathbf{r})|$, respectively. The local ‘magnitude’ of PDW unidirectionality is then defined as

$$F(\mathbf{r}) = \frac{|\Delta_{\mathbf{Q}_x}(\mathbf{r})| - |\Delta_{\mathbf{Q}_y}(\mathbf{r})|}{|\Delta_{\mathbf{Q}_x}(\mathbf{r})| + |\Delta_{\mathbf{Q}_y}(\mathbf{r})|} \quad (4)$$

When $F(\mathbf{r}) > 0$, represented in orange, the PDW along the x direction is dominant, and similarly when $F(\mathbf{r}) < 0$, represented in blue, the PDW order along the y direction is dominant. As shown in Fig. 3c, $F(\mathbf{r})$ is spatially heterogeneous forming a domain structure indicating that the cuprate PDW $\Delta(\mathbf{r})$ is microscopically unidirectional, with one direction predominant in any particular domain. In addition, it appears that the domain size in orange is much bigger than that of blue within the $40 \text{ nm} \times 40 \text{ nm}$ FOV, which may indicate a vestigial nematic²⁸ PDW state, although one cannot be certain without independent knowledge of the shape anisotropy of the nanoflake tip. Overall, these data indicate that the cuprate PDW state is locally strongly unidirectional, and possibly in a vestigial nematic state due to quenched disorder²⁸.

How a coexisting PDW and superconductor induce the CDW modulations

Although the SI-STM technique cannot be used to image a charge density $\rho(\mathbf{r})$ or any of its modulations, a mapping of $g(\mathbf{r}, E)$ and its ratio $Z(\mathbf{r}, E) = g(\mathbf{r}, +E)/g(\mathbf{r}, -E)$ enables one to study how the related $N(\mathbf{r}, E)$ modulates. It has been found that the form-factor symmetry for the induced CDW in cuprates exhibits primarily d -symmetry²⁷. In that case, the CDW modulation does not appear primarily at \mathbf{Q} and $2\mathbf{Q}$ in the Fourier transform of $g(\mathbf{r}, E)$ or $Z(\mathbf{r}, E)$. Instead, to detect the d -symmetry form factor CDW signal at \mathbf{Q} and $2\mathbf{Q}$, one must first use the d -symmetry

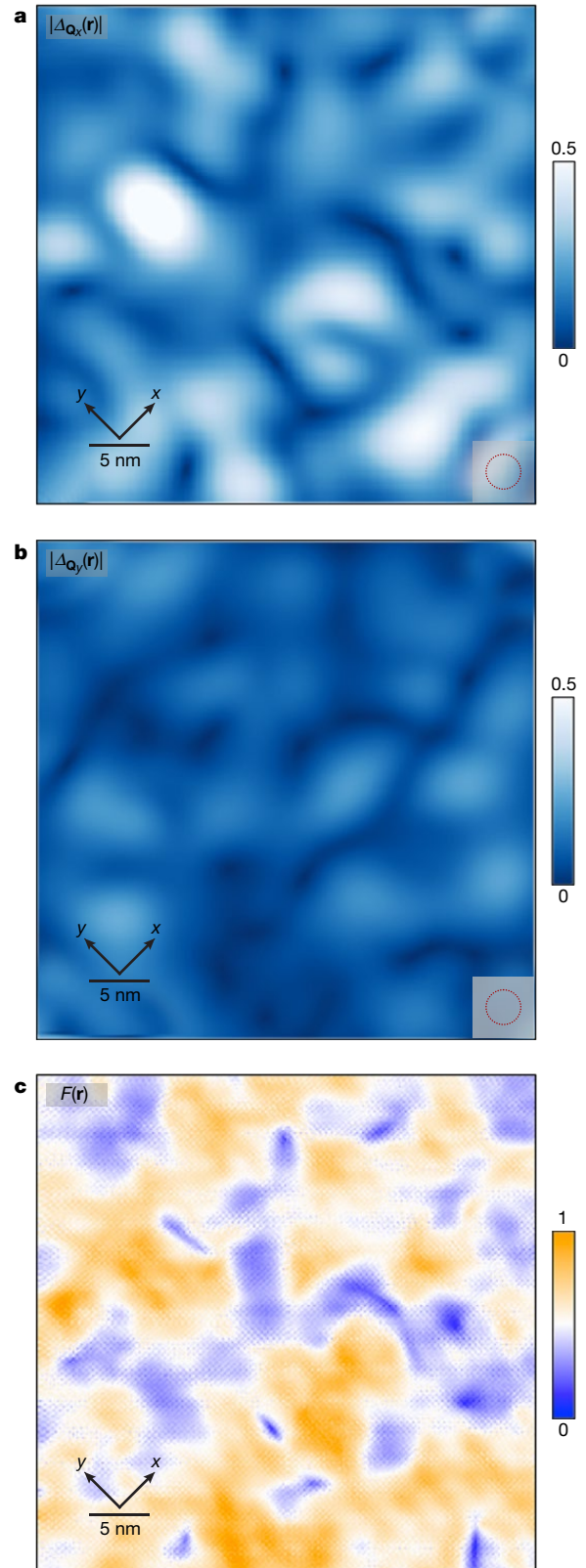


Fig. 3 | The PDW order parameter amplitude and phase. a, The spatial variation of the PDW amplitude $|\Delta_{\mathbf{Q}_x}(\mathbf{r})|$ along the x direction obtained by the two-dimensional lock-in technique. **b**, The spatial variation of the PDW amplitude $|\Delta_{\mathbf{Q}_y}(\mathbf{r})|$ along the y direction obtained by the two-dimensional lock-in technique. The cut-off length is denoted by the broken circle. **c**, The local directionality map defined by equation (4). An orange domain is the region where the PDW amplitude along the x axis is predominant, while a blue domain is the region where the PDW amplitude along the y axis is predominant.

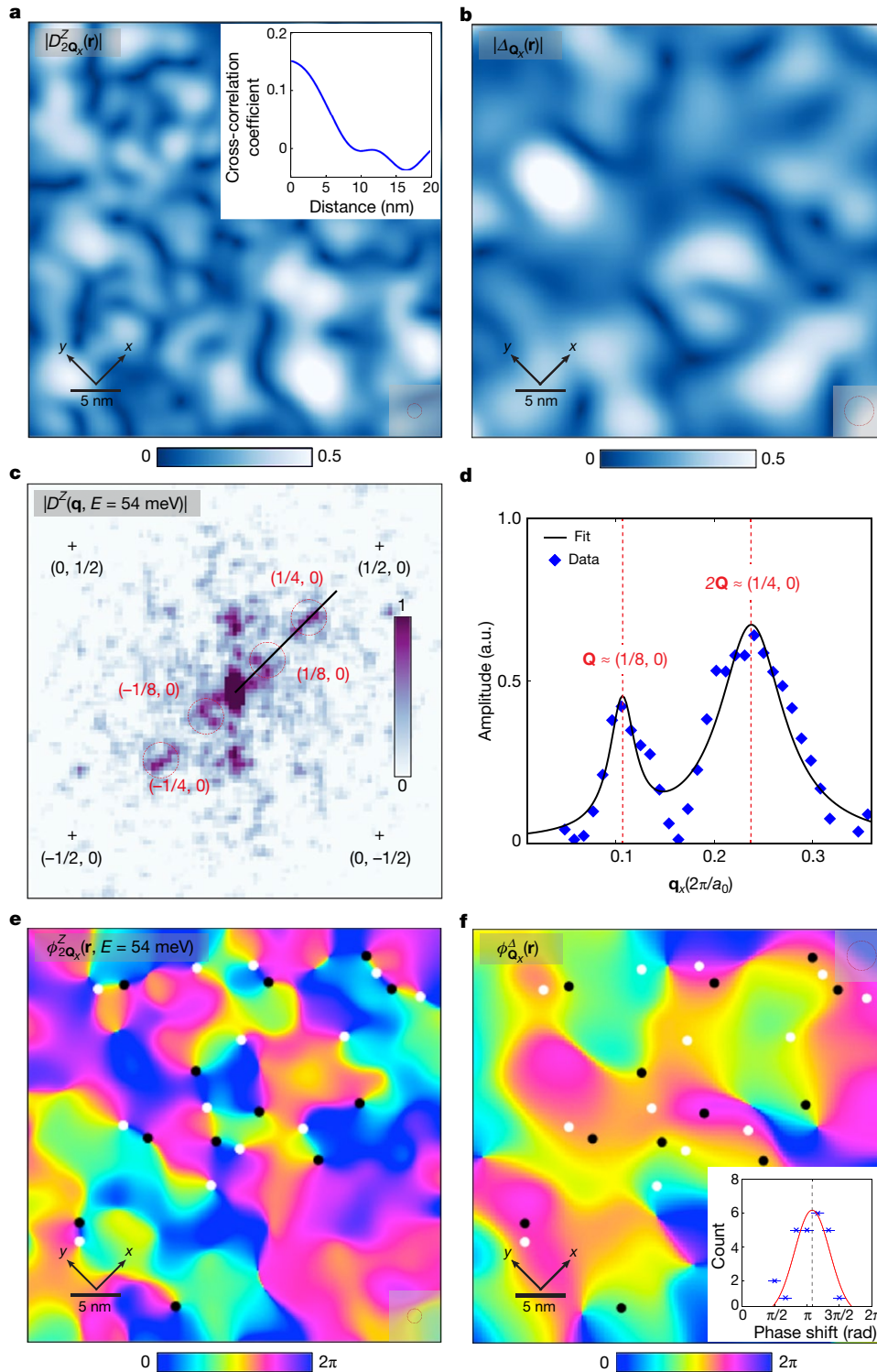


Fig. 4 | The interplay of $N(r)$ and PDW, and the possible half-vortices. **a**, The spatial variation of the $N(r)$ amplitude $D_{2Q_x}^Z(r)$ obtained by equations (1) and (2). The inset shows an azimuthal angular averaged cross-correlation coefficient as a function of distance. **b**, The spatial variation of the $\Delta_{Q_x}(r)$ amplitude obtained by equations (1) and (2). **c**, The magnitude of the phase-resolved Fourier transform, $|D^Z(q)|$ exhibiting both $Q = (2\pi/a_0)(\pm 1/8, 0)$ and $2Q = (2\pi/a_0)(\pm 1/4, 0)$ and peaks encircled by red broken lines, respectively. Coordinates are in units of $2\pi/a_0$. **d**, The line cut of $|D^Z(q)|$, in which the Lorentzian background is subtracted, in **c** from $(2\pi/a_0)(0, 0)$ to $(2\pi/a_0)(\pm 1/4, 0)$, exhibiting well defined peaks at Q and $2Q$. Data points are fitted by Lorentzians and the obtained peak

positions are $(2\pi/a_0)(0.113 \pm 0.002)$ and $(2\pi/a_0)(0.241 \pm 0.003)$ for Q and $2Q$, respectively, with the peak widths $(2\pi/a_0)(0.016 \pm 0.004)$ and $(2\pi/a_0)(0.068 \pm 0.006)$ for Q and $2Q$, respectively. **e**, The spatial phase of the $2QN(r)$ order $\phi_{2Q_x}^Z(r)$ obtained by equation (3). 2π topological defects are marked by solid dots. White (black) dots indicate 2π phase winding along clockwise (anticlockwise). **f**, The spatial phase of the PDW $\phi_{Q_x}^A(r)$. The 2π topological defects in $\phi_{2Q_x}^Z(r)$ from **e** are plotted on top of $\phi_{Q_x}^A(r)$. The inset shows the distribution of $\phi_{Q_x}^A(r)$ values at all the locations where the 2π topological defects in $\phi_{2Q_x}^Z(r)$ are found. The blue crosses are the count and the horizontal bars represent the bin size.

sublattice-phase-resolved Fourier analysis (Methods section ‘Sublattice phase-resolved analysis’). For this reason, we apply a phase-resolved visualization of the d -symmetry modulations to our measured $Z(\mathbf{r}, E)$ (ref. 27), extracting the value of $Z(\mathbf{r}, E)$ at the oxygen sites within each CuO_2 unit cell: $O_x^Z(\mathbf{r}) \equiv Z(\mathbf{r})\delta(\mathbf{r} - \mathbf{r}_{O_x})$ at O_x and similarly for $O_y^Z(\mathbf{r})$ at O_y . We then subtract these values throughout the image to yield

$$D^Z(\mathbf{r}) = O_x^Z(\mathbf{r}) - O_y^Z(\mathbf{r}) \quad (5)$$

In Fig. 4a, b, we show the amplitudes of $|D_{\mathbf{Q}_x}(\mathbf{r})|$ and $|D_{2\mathbf{Q}_x}^Z(\mathbf{r}, E = 54 \text{ meV})|$; systematics of the q -space cut-off length used are discussed in Methods section ‘Cut-off dependence’. If we then consider the magnitude of the Fourier transform of $D^Z(\mathbf{r}, E)$ for $E = 54 \text{ meV}$ where SIS tunnelling has the maximum energy sensitivity (Fig. 1c), a key fact emerges. In the Fourier transform $|D^Z(\mathbf{q}, 54 \text{ meV})|$, we find two strong peaks at \mathbf{Q} and $2\mathbf{Q}$ (Fig. 4c), which are the clearest in these data when presented along the line $(0, 0) - (2\pi/a_0)(0.4, 0)$ in Fig. 4d (from which a Lorentzian background has been subtracted). This complex density wave structure is the expected signature in $N(\mathbf{r}, E)$ modulations^{29–31} of the PDW with wavevector \mathbf{Q} coexisting with the homogeneous SC.

Finally, utilizing the two-dimensional lock-in technique to generate phase-resolved images, the spatial phase $\phi_{2\mathbf{Q}_x}^Z(\mathbf{r}, 54 \text{ meV})$ is extracted using equation (3), and is shown in Fig. 4e. The topological defects with 2π phase winding in the $N(\mathbf{r}, 54 \text{ meV})$ density wave are marked by the black and white dots, for which the winding direction is clockwise and anticlockwise, respectively. The presence of these 2π topological defects in the $N(\mathbf{r}, 54 \text{ meV})$ density wave at $2\mathbf{Q}$ is due microscopically to a dislocation as schematically shown in Fig. 1a (black line). To visualize the interplay of the $2\mathbf{Q}$ density wave and the PDW, the spatial phase $\phi_{\mathbf{Q}_x}^A$ of the PDW order is extracted in the same way, but now at $(2\pi/a_0)(\pm 1/8, 0)$. In Fig. 4f, the locations of the $\phi_{2\mathbf{Q}_x}^Z(\mathbf{r})$ topological defects from Fig. 4e are also plotted on top of the PDW spatial phase $\phi_{\mathbf{Q}_x}^A(\mathbf{r})$. Intriguingly, the $\phi_{2\mathbf{Q}_x}^Z(\mathbf{r})$ topological defects are always found in the vicinity of the yellow strings in $\phi_{\mathbf{Q}_x}^A(\mathbf{r})$, where the PDW phase is π (see Extended Data Fig. 8 for an evolution of the PDW spatial phase). The inset in Fig. 4f shows that the probability distribution of the PDW phase $\phi_{\mathbf{Q}_x}^A$, at which all the topological defects in $\phi_{2\mathbf{Q}_x}^Z(\mathbf{r})$ are found, is clearly centred around π (see Extended Data Fig. 7 for an independent analysis yielding the same conclusion). Thus, the local phase in the PDW surrounding the topological defects in $\phi_{2\mathbf{Q}_x}^Z(\mathbf{r})$ always changes by approximately π (see Extended Data Fig. 8) precisely as expected when a topological defect in the induced density wave at $2\mathbf{Q}$ interacts with the PDW order⁶.

Multiple single-electron signatures of a PDW coexisting with SC

To summarize, use of $\text{Bi}_2\text{Sr}_2\text{CaCu}_2\text{O}_{8+\delta}$ nanoflake scanned tips allows the detection of the spatially modulating energy gap $\Delta(\mathbf{r})$ with eight-unit-cell periodicity, or with axial wavevectors $\mathbf{Q} \approx (2\pi/a_0)(1/8, 0)$ and $\mathbf{Q} \approx (2\pi/a_0)(0, 1/8)$, in superconducting $\text{Bi}_2\text{Sr}_2\text{CaCu}_2\text{O}_{8+\delta}$ (Fig. 2). The spatial analysis of the $\Delta(\mathbf{r})$ modulations shows that they are rather unidirectional within nanoscale domains (Fig. 3). Simultaneous density-of-states imaging reveals two pairs of coexisting $N(\mathbf{r}, E)$ modulations, at wavevectors $\mathbf{Q} \approx (2\pi/a_0)(1/8, 0)$ and $\mathbf{Q} \approx (2\pi/a_0)(0, 1/8)$, and $2\mathbf{Q} \approx (2\pi/a_0)(1/4, 0)$ and $2\mathbf{Q} \approx (2\pi/a_0)(0, 1/4)$ (Fig. 4c, d). Finally, the topological defects in the $N(\mathbf{r}, E)$ density wave at $2\mathbf{Q}$ are concentrated along the lines where the PDW spatial phase changes by π (Fig. 4f). All of these phenomena are canonical signatures^{4,6,28,30,31} of a PDW coexisting with homogeneous SC. Thus, $\Delta(\mathbf{r})$ modulation imaging provides direct spectroscopic evidence of the existence of a PDW, at zero magnetic field in cuprates.

Online content

Any methods, additional references, Nature Research reporting summaries, source data, extended data, supplementary information, acknowledgements, peer review information; details of author contributions and competing interests; and statements of data and code availability are available at <https://doi.org/10.1038/s41586-020-2143-x>.

- Fulde, P. & Ferrel, R. A. Superconductivity in a strong spin-exchange field. *Phys. Rev.* **135**, A550 (1964).
- Larkin, A. I. & Ovchinnikov, Yu. N. Inhomogeneous state of superconductors. *Sov. Phys. JETP* **20**, 762–769 (1965).
- Fradkin, E., Kivelson, S. A. & Tranquada, J. M. Colloquium: theory of intertwined orders in high temperature superconductors. *Rev. Mod. Phys.* **87**, 457–482 (2015).
- Agterberg, D. F. et al. The physics of pair density waves: cuprate superconductors and beyond. Preprint at <https://arxiv.org/abs/1904.09687> (2019).
- Hamidian, M. H. et al. Detection of a Cooper-pair density wave in $\text{Bi}_2\text{Sr}_2\text{CaCu}_2\text{O}_{8+\delta}$. *Nature* **532**, 343–347 (2016).
- Agterberg, D. F. & Tsunetsugu, H. Dislocations and vortices in pair-density-wave superconductors. *Nat. Phys.* **4**, 639–642 (2008).
- Berg, E., Fradkin, E. & Kivelson, S. A. Charge-4e superconductivity from pair-density-wave order in certain high-temperature superconductors. *Nat. Phys.* **5**, 830–833 (2009).
- Norman, M. R., Pines, D. & Kallin, C. The pseudogap: friend or foe of high T_c ? *Adv. Phys.* **54**, 715–733 (2005).
- Li, Q., Hücker, M., Gu, G. D., Tsvetlik, A. M. & Tranquada, J. M. Two-dimensional superconducting fluctuation in stripe-ordered $\text{La}_{1.875}\text{Ba}_{0.125}\text{CuO}_4$. *Phys. Rev. Lett.* **99**, 067001 (2007).
- Berg, E., Fradkin, E., Kivelson, S. A. & Tranquada, J. M. Striped superconductors: how spin, charge, and superconducting orders intertwine in the cuprates. *New J. Phys.* **11**, 115004 (2009).
- Berg, E. et al. Dynamical layer decoupling in a stripe-ordered high- T_c superconductor. *Phys. Rev. Lett.* **99**, 127003 (2007).
- He, R.-H. et al. From a single-band metal to a high-temperature superconductor via two thermal phase transitions. *Science* **331**, 1579–1583 (2011).
- Lee, P. A. Amperean pairing and the pseudogap phase of cuprate superconductors. *Phys. Rev. X* **4**, 031017 (2014).
- Norman, M. R. & Davis, J. C. Quantum oscillations in biaxial pair density wave state. *Proc. Natl Acad. Sci. USA* **115**, 5389–5391 (2018).
- Himeda, A., Kato, T. & Ogata, M. Stripe states with spatially oscillating d -wave superconductivity in the two-dimensional t - t' - J model. *Phys. Rev. Lett.* **88**, 117001 (2002).
- Raczkowski, M., Capello, M., Poilblanc, D., Frésard, R. & Oleś, A. M. Unidirectional d -wave superconducting domains in the two-dimensional t - J model. *Phys. Rev. B* **76**, 140505 (2007).
- Yang, K.-Y., Chen, W. Q., Rice, T. M., Sigrist, M. & Zhang, F.-C. Nature of stripes in the generalized t - J model applied to the cuprate superconductors. *New J. Phys.* **11**, 055053 (2009).
- Loder, F., Graser, S., Kampf, A. P. & Kopp, T. Mean-field pairing theory for the charge-stripe phase of high-temperature cuprate superconductors. *Phys. Rev. Lett.* **107**, 187001 (2011).
- Corboz, P., Rice, T. M. & Troyer, M. Competing states in the t - J model: uniform d -wave state versus stripe state. *Phys. Rev. Lett.* **113**, 046402 (2014).
- Tu, W.-L. & Lee, T.-K. Genesis of charge orders in high temperature superconductors. *Sci. Rep.* **6**, 18675 (2016).
- Choubey, P., Tu, W.-L., Lee, T. K. & Hirschfeld, P. J. Incommensurate charge ordered states in the t - t' - J model. *New J. Phys.* **19**, 013028 (2017).
- Verret, S., Charlebois, M., Sénéchal, D. & Tremblay, A.-M. S. Subgap structures and pseudogap in cuprate superconductors: role of density waves. *Phys. Rev. B* **95**, 054518 (2017).
- Edkins, S. D. et al. Magnetic field-induced pair density wave state in the cuprate vortex halo. *Science* **364**, 976–980 (2019).
- Rajasekaran, S. et al. Probing optically silent superfluid stripes in cuprates. *Science* **359**, 575–579 (2018).
- Mesaros, A. et al. Topological defects coupling smectic modulations to intra-unit-cell nematicity in cuprates. *Science* **333**, 426–430 (2011).
- Fujita, K. et al. in *Strongly Correlated Systems: Experimental Techniques* (eds Avella, A. & Mancini, F.) Ch. 3 (Springer, 2015).
- Fujita, K. et al. Direct phase-sensitive identification of a d -form factor density wave in underdoped cuprates. *Proc. Natl Acad. Sci. USA* **111**, E3026–E3032 (2014).
- Nie, L., Tarjus, G. & Kivelson, S. A. Quenched disorder and vestigial nematicity in the pseudogap regime of the cuprates. *Proc. Natl Acad. Sci. USA* **111**, 7980–7985 (2014).
- Agterberg, D. F. & Garaud, J. Checkerboard order in vortex cores from pair-density-wave superconductivity. *Phys. Rev. B* **91**, 104512 (2015).
- Dai, Z., Zhang, Y.-H., Senthil, T. & Lee, P. A. Pair-density waves, charge-density waves, and vortices in high- T_c cuprates. *Phys. Rev. B* **97**, 174511 (2018).
- Wang, Y. et al. Pair density waves in superconducting vortex halos. *Phys. Rev. B* **97**, 174510 (2018).

© The Author(s), under exclusive licence to Springer Nature Limited 2020

Methods

Sample preparation and measurement

High-quality $\text{Bi}_2\text{Sr}_2\text{CaCu}_2\text{O}_{8+\delta}$ single crystals were grown by the travelling-solvent floating zone method. Here we measured a sample with hole doping level of $p \approx 0.17$. The sample, covered by the Kapton tape, was loaded into the load-lock chamber with pressure better than 3×10^{-10} torr and quickly inserted into the STM head at $T \approx 9$ K, after cleavage by removing the Kapton tape.

Tip preparation and characterization

The tip isotropy is checked by comparing the height of the Bragg peaks for x and y directions in the Fourier transform $T(\mathbf{q})$ of topographic images using the nanoflake tip $T(\mathbf{r})$. A $40 \text{ nm} \times 40 \text{ nm}$ FOV $T(\mathbf{r})$ and its real-part Fourier transform $\text{Re}T(\mathbf{q})$ are shown in Extended Data Fig. 1a, b, respectively. Extended Data Fig. 1c shows line profiles of $\text{Re}T(\mathbf{q})$ along the lines in Extended Data Fig. 1b across the Bragg peaks at (1, 0) and (0, 1). Bragg peak heights at (1, 0) and (0, 1) are found to be comparable within 7%.

Motivation and model for $\Delta(\mathbf{r})$ modulation detection

Motivation of searches for a PDW signature in $\Delta(\mathbf{r})$. Here we discuss preliminary $\Delta(\mathbf{r})$ data, as shown in Extended Data Fig. 4a, c, that motivated and provide reinforcement for the data presented in this study, which is completely independent of them. These data in Extended Data Fig. 4 were acquired with two different $\text{Bi}_2\text{Sr}_2\text{CaCu}_2\text{O}_{8+\delta}$ nanoflake tips, on two different samples, using two different SI-STM instruments. Although experimental conditions were not optimized for detection of $\Delta(\mathbf{r})$ modulations in a PDW, the peaks in $\Delta(\mathbf{q})$ at $\mathbf{Q} = (0, \pm 0.125)$ and $\mathbf{Q} = (0, \pm 0.125)(2\pi/a_0)$ are weakly visible as marked by dashed white circles in Extended Data Fig. 4b, d. Such data, along with those reported in the main text from an experiment designed and optimized for the purpose, provide the type of experimental evidence available on the existence of $8a_0$ modulations in $\Delta(\mathbf{r})$.

Independent pair tunnelling process. Here we discuss how the $4a_0$ modulation observed in the magnitude of the Josephson critical current and the $8a_0$ modulation observed in $\Delta(\mathbf{r})$ in the present study may be linked. We consider a simple model for pair tunnelling from a nanoflake $\text{Bi}_2\text{Sr}_2\text{CaCu}_2\text{O}_{8+\delta}$ tip that is in the coexisting SC and PDW state, to the parallel surface of a bulk $\text{Bi}_2\text{Sr}_2\text{CaCu}_2\text{O}_{8+\delta}$ crystal in the same state (Extended Data Fig. 3). Because the tip is extended and parallel to the surface, the effects of planar tunnelling must be considered. In perfect planar tunnelling, the $c_k^\dagger c_{-k}^\dagger$ Cooper pairs of the homogenous SC cannot tunnel into the $c_k^\dagger c_{-k+Q}^\dagger$ Cooper pairs of the PDW, because that violates conservation of momentum. In that limit, the Josephson current I_J from a $\text{Bi}_2\text{Sr}_2\text{CaCu}_2\text{O}_{8+\delta}$ extended tip to the $\text{Bi}_2\text{Sr}_2\text{CaCu}_2\text{O}_{8+\delta}$ crystal is composed of two independent contributions: I_J^S due to pair tunnelling from $c_k^\dagger c_{-k}^\dagger$ to $c_k^\dagger c_{-k}^\dagger$ states, and I_J^P due to pair tunnelling from $c_k^\dagger c_{-k+Q}^\dagger$ to $c_k^\dagger c_{-k+Q}^\dagger$ states.

Consider two PDW, one in the nanoflake tip ψ_T and one in the sample ψ_S , with order parameters

$$\psi_T = \Delta_1 e^{i\theta_1} (e^{i(Qx+\delta)}) \text{ and } \psi_S = \Delta_2 e^{i\theta_2} (e^{iQx})$$

where x is the position and θ is the phase of the order parameter. The Josephson coupling will be of the form $K(\psi_T \psi_S^* + \psi_T^* \psi_S) \propto \cos(\theta_1 - \theta_2) \cos(Q\delta)$ where K is a constant and δ is the variable spatial displacement of the tip PDW relative to the sample PDW. In this case, the inter-PDW Josephson current takes the form

$$I_J^P \propto \sin(\theta_1 - \theta_2) \sin(Q\delta)$$

It is the magnitude $|I_J^P|$ that is measured as a function of transverse displacement δ between nanoflake tip and sample where $Q = 2\pi/\lambda$ and λ a

wavelength, and this obviously modulates as $|I_J^P| \propto |\sin(Q\delta)|$ or with a periodicity of $\lambda/2$.

Our previous studies using scanned Josephson tunnelling³² actually measured the magnitude of the Josephson current $|I_J|$. Thus, if I_J^S and I_J^P are independent, then $|I_J| = |I_J^S| + |I_J^P|$. Assuming that $|I_J^S|$ is roughly constant spatially, then $|I_J^P| \propto |\sin(Q\delta)|$, where δ is the transverse displacement between the PDW in the extended tip and the PDW in the sample. Therefore, in this model for our experiment, if the PDW has true periodicity $8a_0$ then its gap modulation $\Delta(\mathbf{r})$ will necessarily have periodicity $8a_0$ but, critically, the modulations in magnitude of the total Josephson current $|I_J|$ will have periodicity $4a_0$.

Note that if there are two strictly independent unidirectional PDWs with wavevectors \mathbf{Q}_x and \mathbf{Q}_y , and Cooper pair momentum of each is conserved, then the \mathbf{Q}_x PDW cannot tunnel to the \mathbf{Q}_y PDW and vice versa. This would pose a challenge to the above analysis. However, if the PDW state in the tip is somewhat biaxial (for example, ref.³³), then this analysis would retain validity.

Effect of structural supermodulation on measured $\Delta(\mathbf{r})$. One might ask whether there is an effect of the crystal supermodulation with $\mathbf{Q}_{\text{SM}} \parallel (1, 1)(2\pi/a_0)$ that produces an energy gap modulation at its wavevector, on our measured $\Delta(\mathbf{r})$. As we reported in ref.⁵, we observed the modulations both in $\Delta(\mathbf{r})$ and the Josephson critical current at \mathbf{Q}_{SM} . However, this is a trivial effect and its wavevector is at 45° degrees off the Cu–O–Cu direction. Most importantly, a spatial convolution between the tip and sample of their modulating $\Delta(\mathbf{r})$ at \mathbf{Q}_{SM} cannot produce any additional modulations at different wavevectors. Thus, the effect of structural supermodulation does not produce any other gap modulation signals, especially at $\mathbf{Q} = (0, \pm 0.125)$ and $\mathbf{Q} = (0, \pm 0.125)(2\pi/a_0)$.

Effect of $\Delta(\mathbf{r})$ on nanoflake. Here we discuss how $\Delta(\mathbf{r})$ modulation detection is enhanced in $\text{Bi}_2\text{Sr}_2\text{CaCu}_2\text{O}_{8+\delta}$ nanoflake SIS tunnelling. Here the measured $\Delta(\mathbf{r})$ can be regarded as a consequence of a spatial convolution between the sample and nanoflake PDW order parameters. The nanoflake is most likely in the same PDW state as it is picked up from the same sample. Thus, the order parameter on the nanoflake is approximated in a form of $\Delta_{\text{nanoflake}} \exp(i\mathbf{Q}_p \cdot \mathbf{r}) \exp\left(-\frac{r^2}{2\sigma^2}\right)$, where the exponential term is approximated to represent a nanoflake structure factor with size of nanoflake (about 3 nm, see Extended Data Fig. 2). This acts as a low-pass filter in the convolution between gap modulations at the same wavevector \mathbf{Q}_p in the tip and in the sample. Such a convolution effect naturally works as a 'lock-in', mitigating the signals unrelated to the gap modulation wavevector \mathbf{Q}_p . This process makes the signal of $\Delta(\mathbf{r})$ modulation detectable.

Data analysis

Sublattice phase-resolved analysis. To reveal any possible local-density-of-states $N(\mathbf{r}, E)$ modulations, we analyse differential conductance $g(\mathbf{r}, E)$ to yield $Z(\mathbf{r}, E) = g(\mathbf{r}, +E)/g(\mathbf{r}, -E)$ (Extended Data Fig. 5 and ref.²⁶). Intensities at oxygen sites \mathbf{r}_O and \mathbf{r}_O are extracted separately from $Z(\mathbf{r}, E = 54 \text{ meV})$ and used to form two new maps, $O_x^Z(\mathbf{r}, E = 54 \text{ meV})$ and $O_y^Z(\mathbf{r}, E = 54 \text{ meV})$, respectively. We then calculate each sublattice-phase-resolved $Z(\mathbf{r}, E)$ image and separate it into three: the first, $\text{Cu}(\mathbf{r})$, contains only the measured values of $Z(\mathbf{r})$ at Cu sites while the other two, $O_x(\mathbf{r})$ and $O_y(\mathbf{r})$, contain only the measurements at the x -/ y -axis oxygen sites.

Phase-resolved Fourier transforms of the $O_x(\mathbf{r})$ and $O_y(\mathbf{r})$ sublattice images $\tilde{O}_x(\mathbf{q}) = \text{Re}\tilde{O}_x(\mathbf{q}) + i\text{Im}\tilde{O}_x(\mathbf{q})$; $\tilde{O}_y(\mathbf{q}) = \text{Re}\tilde{O}_y(\mathbf{q}) + i\text{Im}\tilde{O}_y(\mathbf{q})$, are used to determine the form factor symmetry for modulations at any \mathbf{q}

$$\tilde{D}^Z(\mathbf{q}) = (\tilde{O}_x(\mathbf{q}) - \tilde{O}_y(\mathbf{q}))/2$$

$$\tilde{S}^Z(\mathbf{q}) = (\tilde{O}_x(\mathbf{q}) + \tilde{O}_y(\mathbf{q}))/2$$

$$\tilde{S}^Z(\mathbf{q}) = \widetilde{Cu}(\mathbf{q})$$

Specifically, for a density wave occurring at \mathbf{Q} , one can then evaluate the magnitude of its d -symmetry form factor $\tilde{D}(\mathbf{Q})$ and its s' - and s -symmetry form factors $\tilde{S}'(\mathbf{Q})$ and $\tilde{S}(\mathbf{Q})$, respectively. In terms of the segregated sublattices, a d -form factor density wave is one for which the density wave on the O_x sites is in antiphase with that on the O_y sites. Studies of electronic structure in underdoped $\text{Bi}_2\text{Sr}_2\text{CaCu}_2\text{O}_{8+x}$ and $\text{Ca}_{2-x}\text{Na}_x\text{CuO}_2\text{Cl}_2$ consistently exhibit a relative phase of π and therefore a d -symmetry form factor.

Hence the peaks at $\pm\mathbf{Q}_x$ and $\pm\mathbf{Q}_y$ present in both $\tilde{O}_x(\mathbf{q})$ and $\tilde{O}_y(\mathbf{q})$ must cancel exactly in $\tilde{O}_x(\mathbf{q}) + \tilde{O}_y(\mathbf{q})$. Therefore, if a density wave at \mathbf{Q} and $2\mathbf{Q}$ has predominantly d -symmetry form factor, there is no detectable signal in $g(\mathbf{r}, E)$ or $Z(\mathbf{r}, E)$ at \mathbf{Q} and $2\mathbf{Q}$, and why the d -symmetry Fourier transform $D^g(\mathbf{q}, E)$ or $D^Z(\mathbf{q}, E)$ are used in these studies. Specifically, by calculating $D^Z(\mathbf{q}) = \text{FFT}(D^Z(\mathbf{r}))$ one correctly extracts the d -symmetry density wave modulations that are occurring at \mathbf{Q} and $2\mathbf{Q}$.

Cut-off dependence. Here we show how the images shown in Fig. 4 evolve as a function of cut-off length used in the two-dimensional lock-in technique. In Extended Data Fig. 6, both $D_{2\mathbf{Q}_x}^Z(\mathbf{r}, 54 \text{ meV})$ and $\Delta_{\mathbf{Q}_x}(\mathbf{r})$ are shown at different real-space cut-off lengths: 8, 16, 24, 32 and 40 Å. In the left column, we can see a big change between 8 and 16 Å in the spatial structure of $|D_{2\mathbf{Q}_x}^Z(\mathbf{r})|$ as oscillatory components are vanished, while $|D_{2\mathbf{Q}_x}^Z(\mathbf{r})|$ at 16, 24, 32 and 40 Å are virtually identical. For $\Delta_{\mathbf{Q}_x}(\mathbf{r})$ in the right column in Extended Data Fig. 6, the oscillatory components are gone between 16 and 24 Å. Thus, the cut-off lengths used in Fig. 3, 16 and 40 Å, do not introduce erroneous oscillations by picking up irrelevant contributions from other wavevectors and are reasonable choices.

Interplay of the eight-unit-cell periodic PDW and the four-unit-cell induced $N(\mathbf{r}, E)$ modulation. To support the Fig. 4f inset, in which 2π topological defects in the induced $N(\mathbf{r})$ modulation at $2\mathbf{Q}$ tends to be found in the vicinity of the locus of π phase in $\Phi_{\mathbf{Q}_x}^A(\mathbf{r})$ (yellow strings), we performed an independent analysis: the distances of the white and black dots to the nearest position on the yellow strings are calculated and compared with randomly distributed results. Extended Data Fig. 7a shows the distance distribution of the total 25 topological defects in Fig. 4e. Then we generate randomly distributed 25 'topological defects' inside the same FOV and calculate distances to the same yellow strings, and this process has been repeated 100 times. The average result of the 100 different configurations is shown in Extended Data Fig. 7b.

It is clear that the distribution from the measured $N(\mathbf{r})$ topological defects at $2\mathbf{Q}$ is in a smaller range with higher magnitude compared with random results. This supports that the topological defects in the measured $N(\mathbf{r})$ modulation at $2\mathbf{Q}$ actually show a statistically strong tendency to be found near the locus of π phase in $\Phi_{\mathbf{Q}_x}^A(\mathbf{r})$.

π phase winding and possible half-vortex in PDW. In search for half-vortices in PDW, we analysed PDW phase $\Phi_{\mathbf{Q}_x}^A(\mathbf{r})$ in the vicinity of the 2π topological defects from the induced $N(\mathbf{r})$ modulation at $2\mathbf{Q}$. We extracted the values along each contour surrounding the 2π topological defects from the induced $N(\mathbf{r})$ modulation at $2\mathbf{Q}$ (Extended Data Fig. 8a) and plotted an evolution of the PDW phase for each contour in Extended Data Fig. 8b. Although no singularities that have a π phase winding in $\Phi_{\mathbf{Q}_x}^A(\mathbf{r})$ are found, indeed PDW phases are changing by π along each contour, indicating the presence of possible half-vortices.

Data availability

The data that support the findings of this study are available from the corresponding author upon reasonable request.

32. Cho, D. et al. A strongly inhomogeneous superfluid in an iron-based superconductor. *Nature* **571**, 541–545 (2016).
33. Norman, M. R. & Davis, J. C. Quantum oscillations in a biaxial pair density wave state. *Proc. Natl Acad. Sci. USA* **115**, 5389–5391 (2018).

Acknowledgements We thank S. D. Edkins, E. Fradkin, M. H. Hamidian, S. A. Kivelson, P. A. Lee and J. M. Tranquada, for discussions and advice. Z.D., H.L., K.F. G.G. and P.D.J. acknowledge support from the US Department of Energy, Office of Basic Energy Sciences, under contract number DEAC02-98CH10886. S.H.J. and J.L. acknowledge support from the Institute for Basic Science in Korea (grant number IBS-R009-G2), the Institute of Applied Physics of Seoul National University and a National Research Foundation of Korea (NRF) grant funded by the Korea government (MSIP) (number 2017R1A2B3009576). E.P.D. was supported by the Brookhaven National Laboratory Supplemental Undergraduate Research Program (SURP). J.C.S.D. acknowledges support from the Science Foundation of Ireland under award SFI 17/RP/5445 and from the European Research Council (ERC) under award DLV-788932.

Author contributions K.F. designed and led the project. Z.D., H.L., S.H.J., E.P.D. and K.F. carried out experiments at the MIRAGE STM of the OASIS complex at Brookhaven National Laboratory; G.G. synthesized and characterized the samples; Z.D., H.L. and K.F. developed and carried out analysis. K.F. wrote the paper with key contributions from J.C.S.D., Z.D., H.L., J.L. and P.D.J. The manuscript reflects the contributions and ideas of all authors.

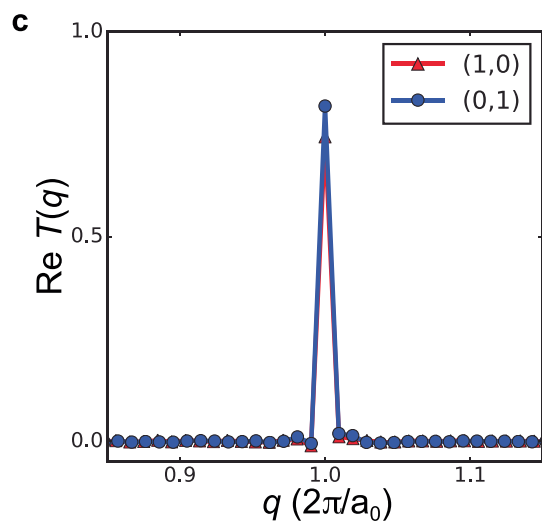
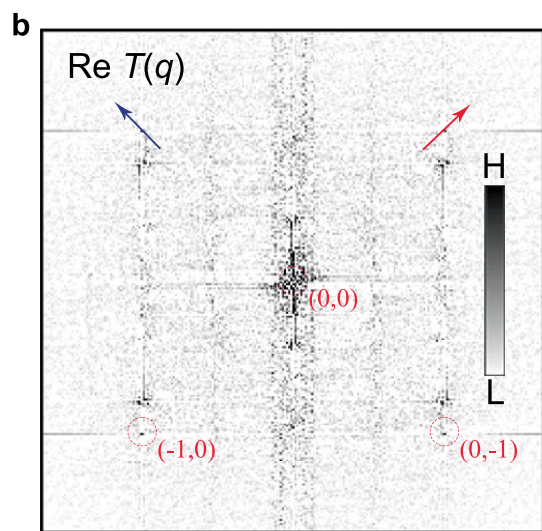
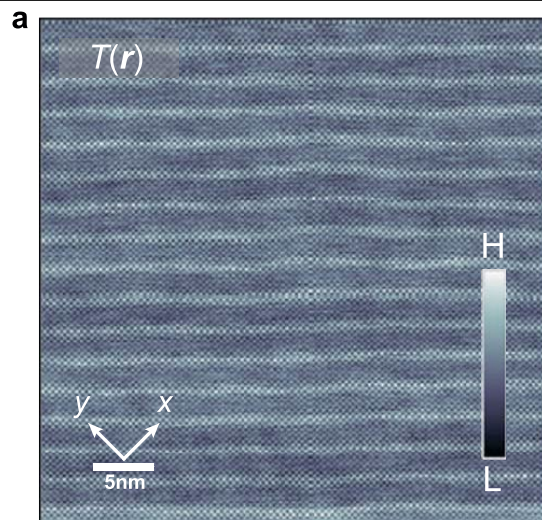
Competing interests The authors declare no competing interests.

Additional information

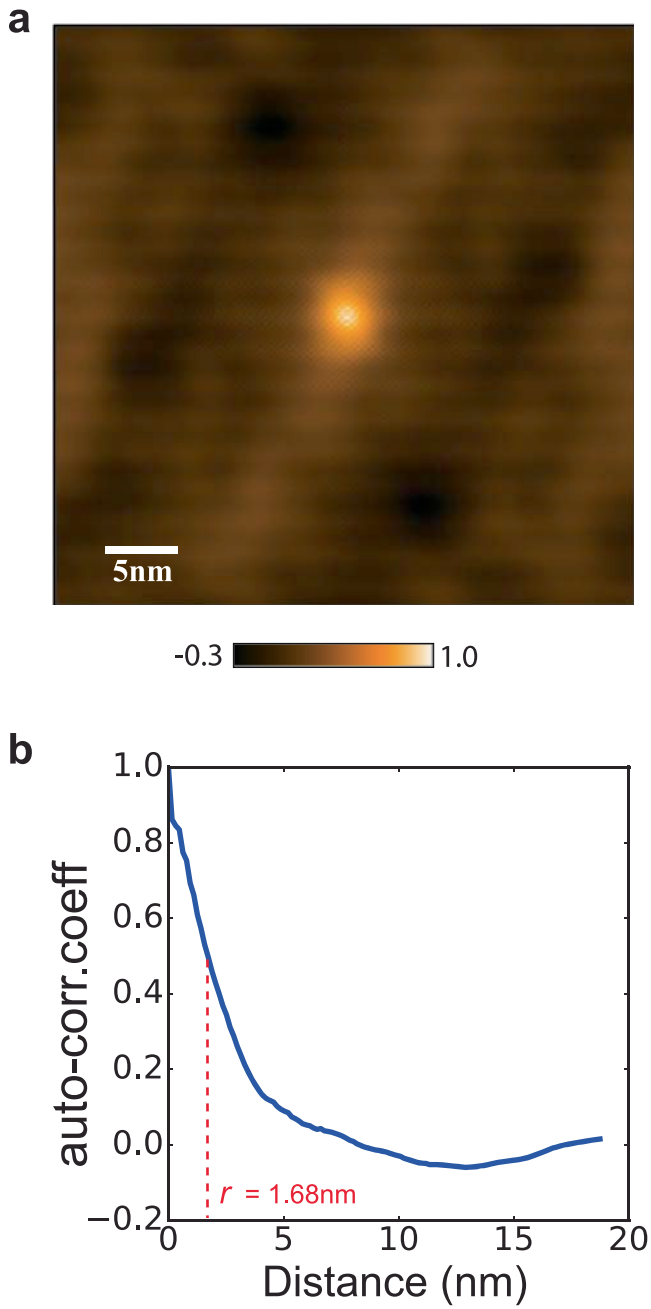
Correspondence and requests for materials should be addressed to K.F.

Peer review information *Nature* thanks Ting-Kuo Lee, Yi Yin and the other, anonymous, reviewer(s) for their contribution to the peer review of this work.

Reprints and permissions information is available at <http://www.nature.com/reprints>.

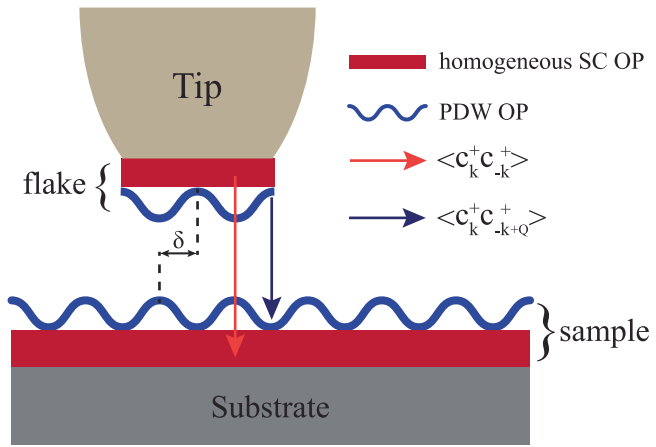


Extended Data Fig. 1 | Analysis of the tip isotropy. **a**, Topography $T(r)$ within $40 \text{ nm} \times 40 \text{ nm}$ FOV. **b**, Real part of Fourier transform of $T(r)$. **c**, Line profile $\text{Re } T(q)$ along the line in the middle panel, representing nearly equal Bragg peak height (difference is less than 7%).

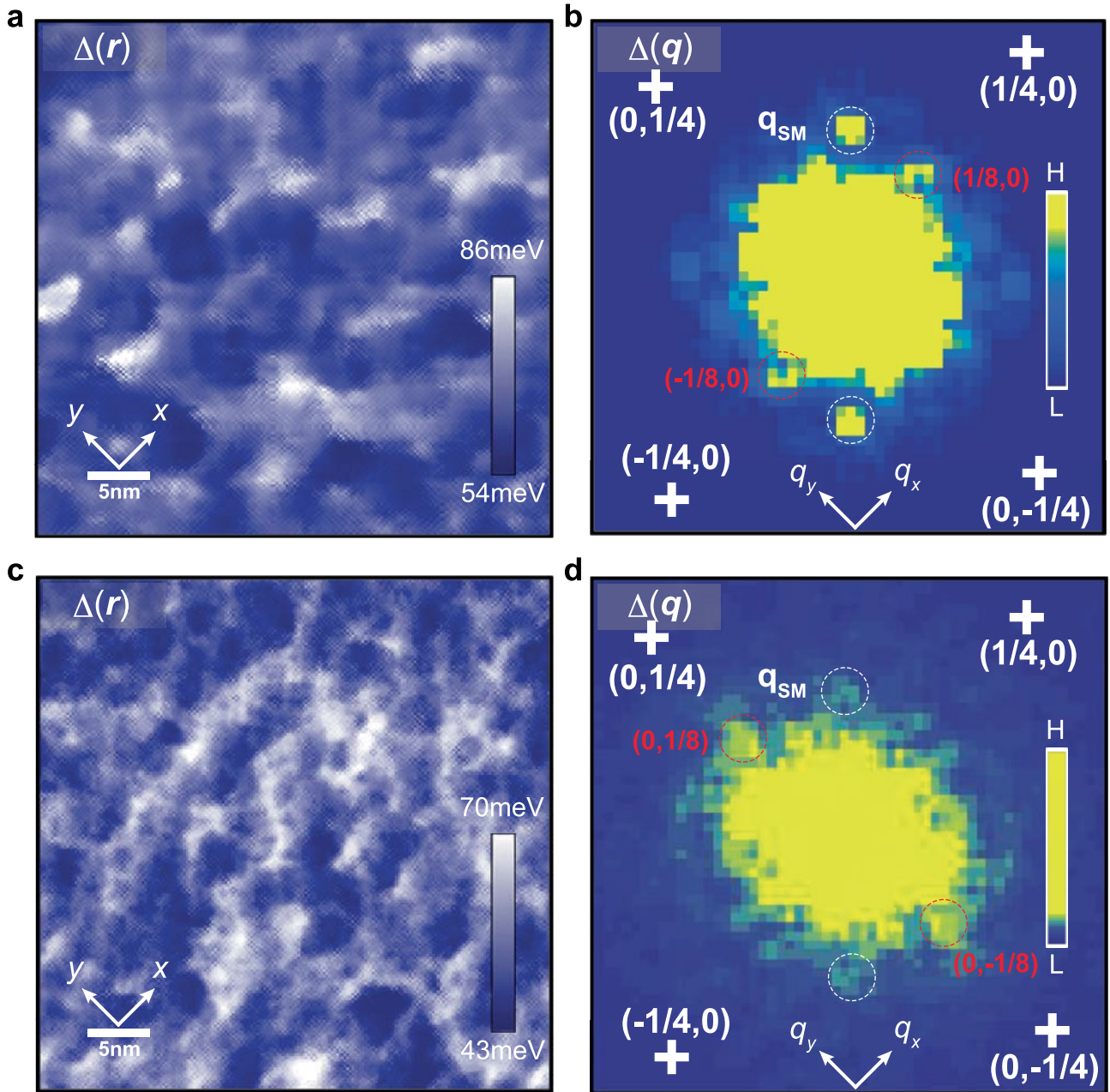


Extended Data Fig. 2 | Estimation of the nanoflake tip geometry.

a, Autocorrelation of $\Delta(\mathbf{r})$. **b**, Line profile measured from centre in **a** is azimuthal-angle averaged. The size of the nanoflake on the tip is estimated from the full-width at half-maximum and is around 3.3 nm.

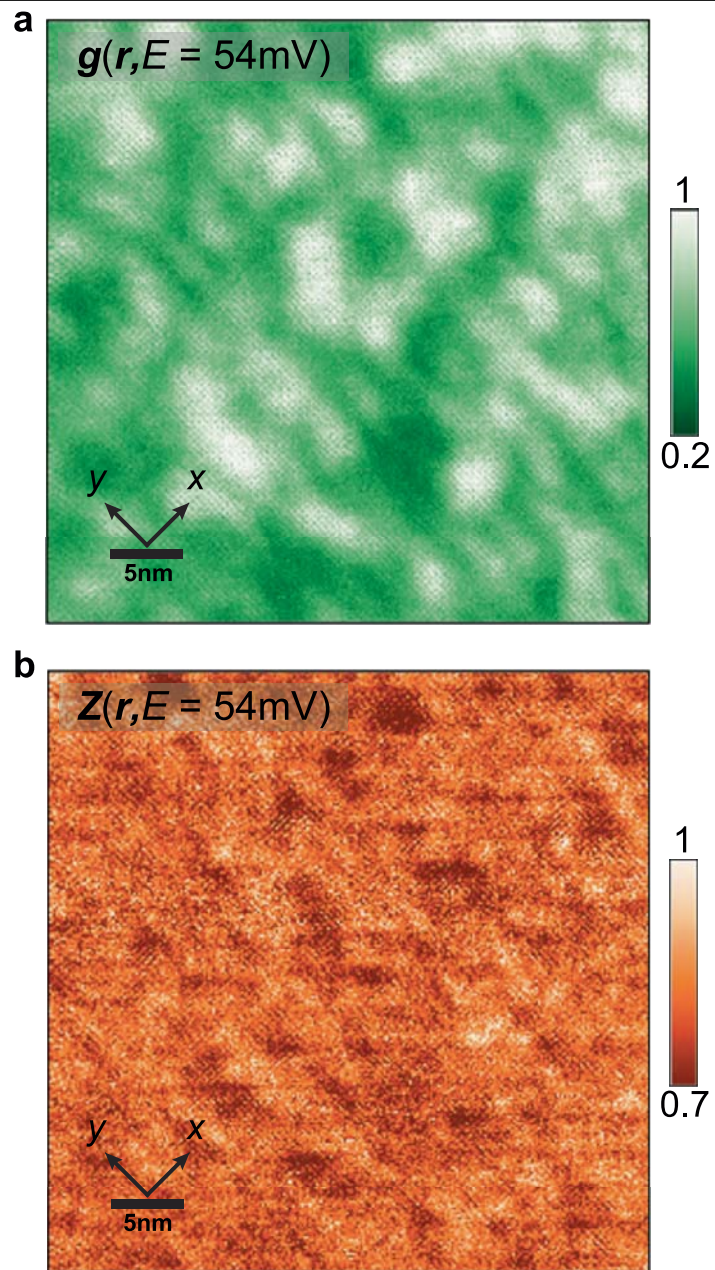


Extended Data Fig. 3 | Possible process of the Josephson tunnelling.
 Schematic representation of planar Josephson tunnelling in the presence of two order parameters (OPs): homogeneous SC and PDW.

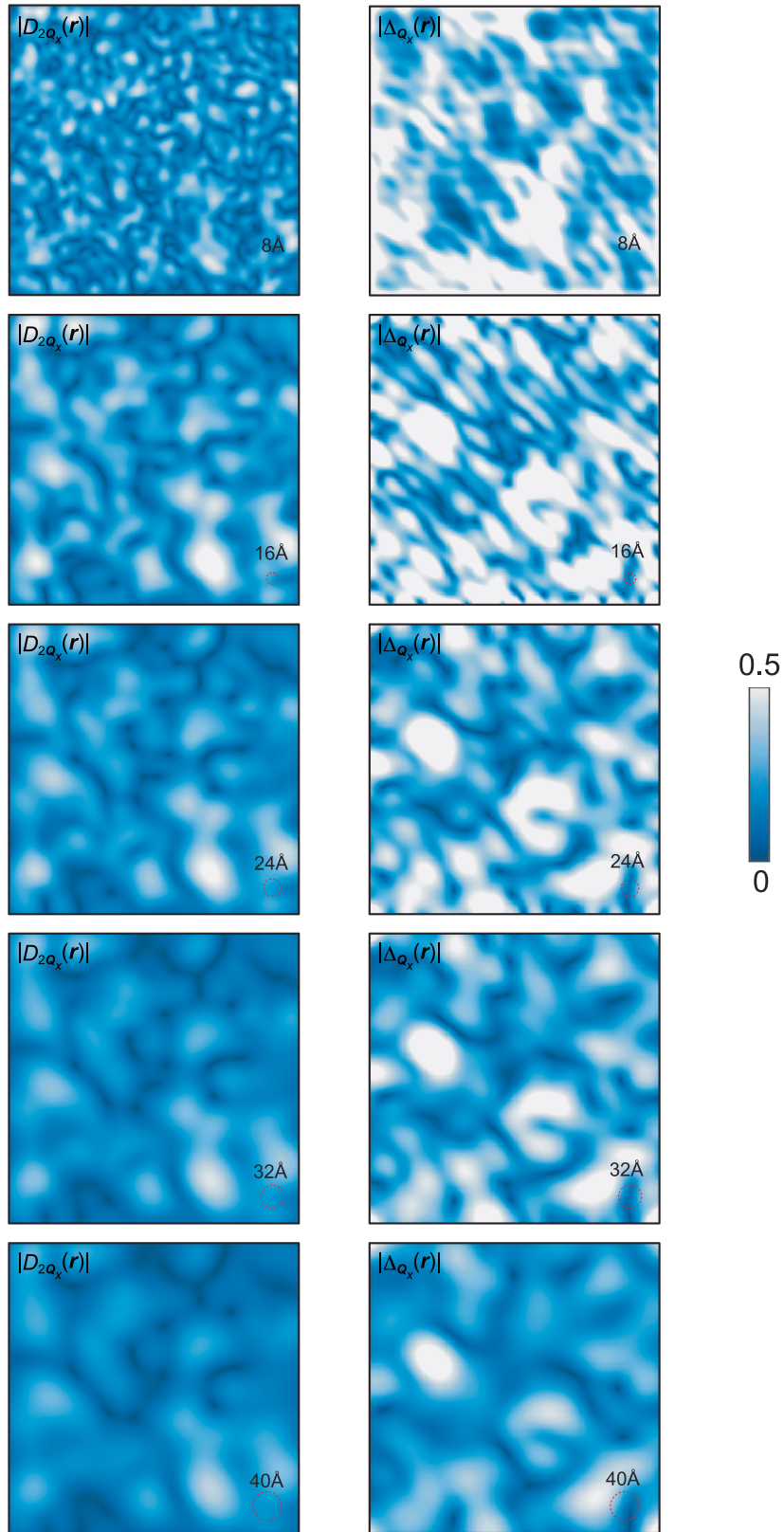


Extended Data Fig. 4 | Preliminary experimental data analysis.
a, c, Preliminary $\Delta(r)$ independently measured at 4.2 K on different pieces of nearly optimally doped $\text{Bi}_2\text{Sr}_2\text{CaCu}_2\text{O}_{8+\delta}$. **b, d,** The magnitude of Fourier

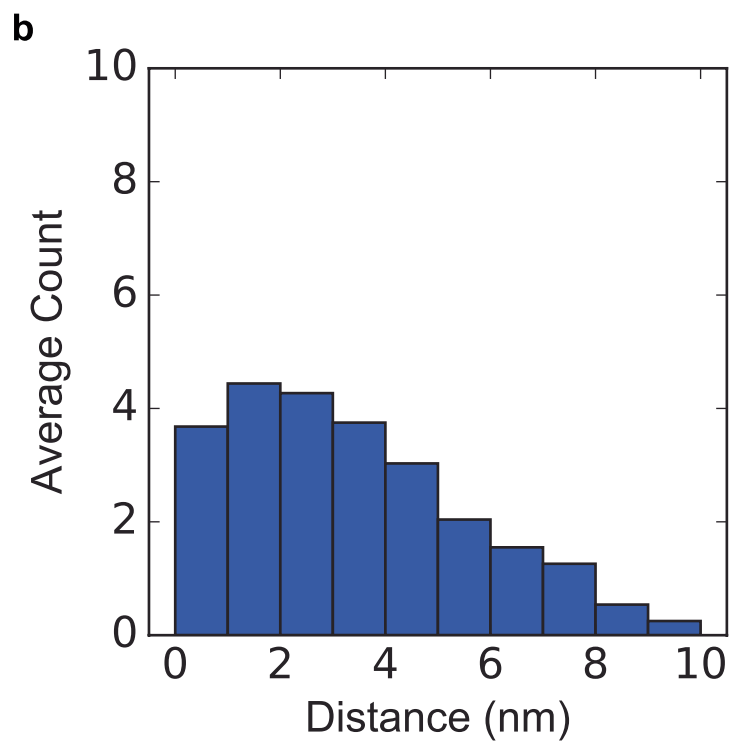
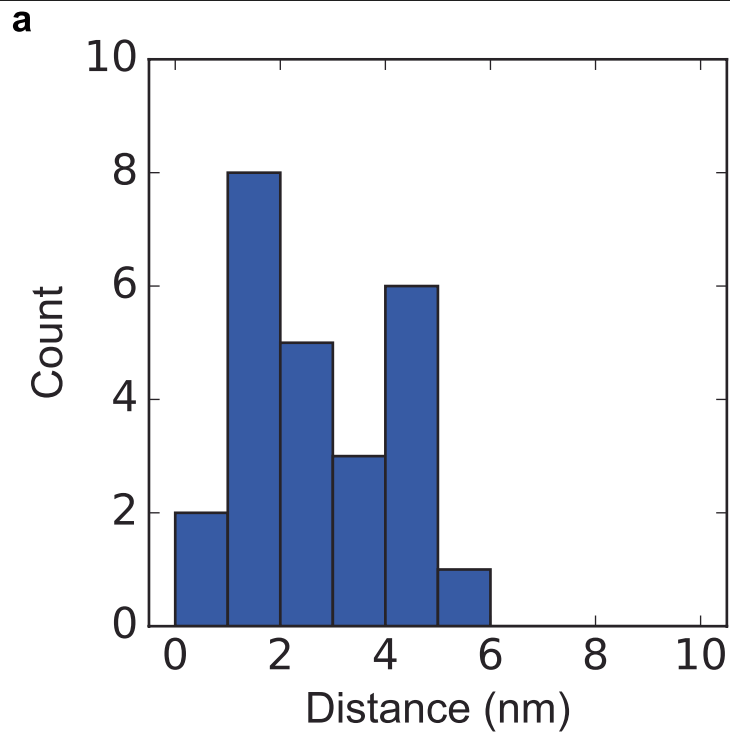
transform of $\Delta(r)$ in **a** and **c**, respectively, representing early observations of $1/8$ peaks marked by the red circles.



Extended Data Fig. 5 | Differential conductance map and its ratio. **a**, $g(r, E = 54 \text{ meV})$ map. The eight-unit-cell CDW modulation, that is, the PDW induced $N(\mathbf{r})$ modulation at \mathbf{Q} , can be seen. **b**, $Z(r, E = 54 \text{ meV})$ calculated by $Z(r, E) = g(r, E)/g(r, -E)$.

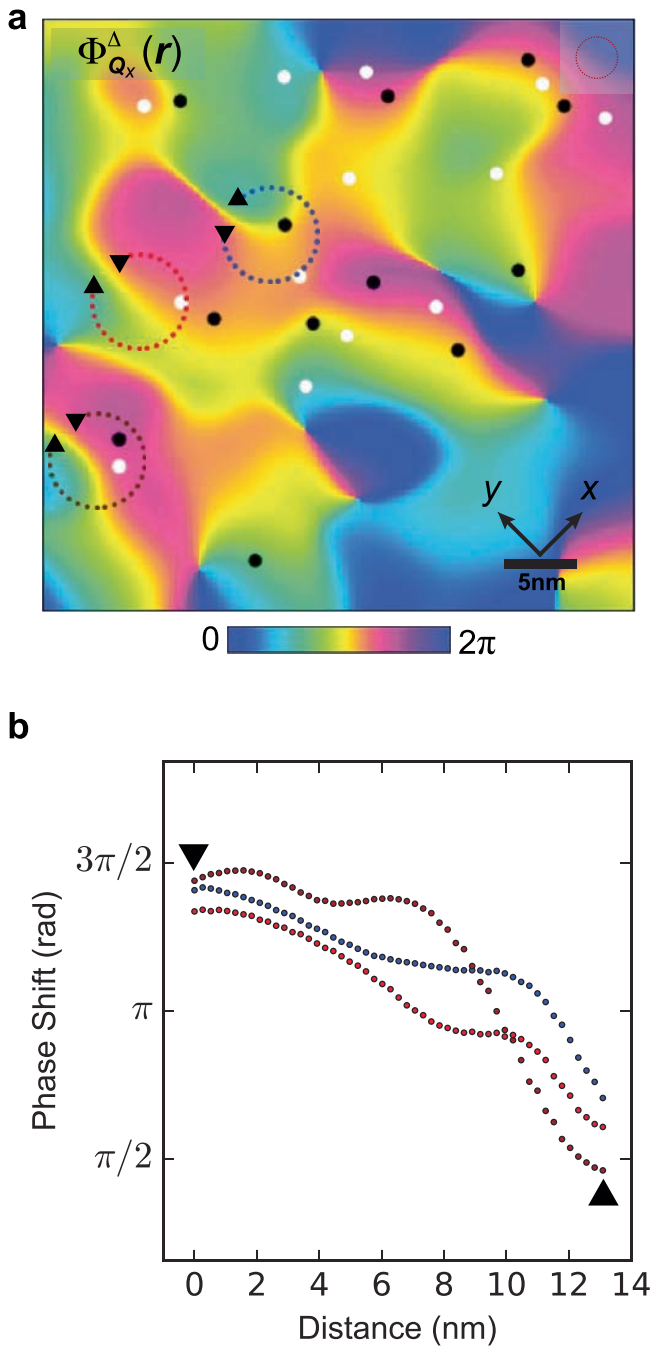


Extended Data Fig. 6 | Cut-off length dependence of $|D_{2Q_x}^Z(r)|$ and $|\Delta_{Q_x}(r)|$. The left column shows $|D_{2Q_x}^Z(r)|$ at different cut-off lengths, similarly for the right column for $|\Delta_{Q_x}(r)|$.



Extended Data Fig. 7 | Distance analysis. a. A count distribution sorted by distances between the topological defects in the induced $N(\mathbf{r})$ modulation at $2\mathbf{Q}$ from Fig. 4b and the nearest point on the yellow strings in the PDW phase

map from Fig. 4c. **b.** Average distribution of 100 configurations, within each configuration 25 points are randomly generated in the same FOV and distances to the same yellow strings are calculated and sorted.



Extended Data Fig. 8 | Spatial evolution of the PDW phase. a, A phase map $\Phi_{Q_x}^\Delta(r)$ of the PDW order. Three representative contours surrounding the 2π topological defects from $\Phi_{2Q_x}^\Delta(r)$ across the yellow strings. **b,** An evolution of the phase along each contour in **a**. The upside-down black triangle marks the starting point of winding and the upright black triangle marks the ending point, in correspondence with the winding directions in **a**. π phase windings are clearly seen in the PDW phase surrounding the 2π topological defects from $\Phi_{2Q_x}^\Delta(r)$.